



Article

A Core–Shell Au@TiO₂ and Multi-Walled Carbon Nanotube-Based Sensor for the Electroanalytical Determination of H₂O₂ in Human Blood Serum and Saliva

Ayman Ali Saeed ¹, Mohammed Nooredeen Abbas ¹, Waheed Fathi El-Hawary ², Yousry Moustafa Issa ² and Baljit Singh ^{3,*}

¹ Applied Organic Chemistry Department, Chemical Industries Research Institute, National Research Centre (NRC), Dokki, Giza 12622, Egypt

² Chemistry Department, Faculty of Science, Cairo University, Giza 12613, Egypt

³ MiCRA Biodiagnostics Technology Gateway & Centre of Applied Science for Health, Technological University Dublin (TU Dublin), D24 FKT9 Dublin 24, Ireland

* Correspondence: baljit.singh@tudublin.ie; Tel.: +353-12-207-863

Abstract: A hydrogen peroxide (H₂O₂) sensor was developed based on core–shell gold@titanium dioxide nanoparticles and multi-walled carbon nanotubes modified glassy carbon electrode (Au@TiO₂/MWCNTs/GCE). Core–shell Au@TiO₂ material was prepared and characterized using a scanning electron microscopy and energy dispersive X-ray analysis (SEM/EDX), transmission electron microscopy (TEM), atomic force microscopy (AFM), Raman spectroscopy, X-ray diffraction (XRD) and Zeta-potential analyzer. The proposed sensor (Au@TiO₂/MWCNTs/GCE) was investigated electrochemically using cyclic voltammetry (CV) and electrochemical impedance spectroscopy (EIS). The analytical performance of the sensor was evaluated towards H₂O₂ using differential pulse voltammetry (DPV). The proposed sensor exhibited excellent stability and sensitivity with a linear concentration range from 5 to 200 μM ($R^2 = 0.9973$) and 200 to 6000 μM ($R^2 = 0.9994$), and a limit of detection (LOD) of 1.4 μM achieved under physiological pH conditions. The practicality of the proposed sensor was further tested by measuring H₂O₂ in human serum and saliva samples. The observed response and recovery results demonstrate its potential for real-world H₂O₂ monitoring. Additionally, the proposed sensor and detection strategy can offer potential prospects in electrochemical sensors development, indicative oxidative stress monitoring, clinical diagnostics, general cancer biomarker measurements, paper bleaching, etc.

Keywords: electrochemical sensor; core–shell; titanium dioxide; gold nanoparticles; carbon nanotubes; hydrogen peroxide



Citation: Saeed, A.A.; Abbas, M.N.; El-Hawary, W.F.; Issa, Y.M.; Singh, B. A Core–Shell Au@TiO₂ and Multi-Walled Carbon Nanotube-Based Sensor for the Electroanalytical Determination of H₂O₂ in Human Blood Serum and Saliva. *Biosensors* **2022**, *12*, 778. <https://doi.org/10.3390/bios12100778>

Received: 19 August 2022

Accepted: 15 September 2022

Published: 20 September 2022

Publisher's Note: MDPI stays neutral with regard to jurisdictional claims in published maps and institutional affiliations.



Copyright: © 2022 by the authors. Licensee MDPI, Basel, Switzerland. This article is an open access article distributed under the terms and conditions of the Creative Commons Attribution (CC BY) license (<https://creativecommons.org/licenses/by/4.0/>).

1. Introduction

Carbon nanomaterials, including single-walled carbon nanotubes (SWCNTs), multi-walled carbon nanotubes (MWCNTs), nanofibers, activated carbon and graphene, have unique properties such as chemical stability and durability, high electrical conductivity, mechanical strength and a high surface-to-volume ratio which collectively makes them an excellent choice for electrochemical sensors and biosensors development [1–10]. Carbon nanotubes (CNTs) are an excellent and promising option in fabricating electrochemical sensors owing to their remarkable electrical and thermal conductivity, high surface area, chemical stability and mechanical properties [11–14]. Metal nanoparticles, due to their excellent conductivity, surface area and remarkable electrocatalytic properties, are considered ideal candidates for the electrochemical detection of hydrogen peroxide (H₂O₂). They are capable of promoting electron transfer processes and offer abundant catalytic active sites during the H₂O₂ redox reaction. Carbon-based nanomaterials can be mixed with metal nanoparticles to create composites that have excellent synergistic features, which can improve the sensitivity and overall performance of the modified electrodes.

Core-shell nanomaterials (CSNs) are composite materials with a core-shell structure formed by an inner layer of one material (core) and an exterior layer of another material (shell) [15]. The shell materials are frequently chosen based on their nature and the targeted application. Many advantages can be achieved by carefully selecting shell material, including improved optical/electrical/magnetic properties, multifunctional capability, thermal stability or dispersibility of the materials, reduced precious material content and efficient use. In the core-shell structure, the size and kind of core are also crucial factors. The main advantage of CSNs is that the distinct properties of the core and shell can be combined in a single material, resulting in improved electrocatalytic activity and new physical and chemical properties that are inaccessible or unavailable from the individual components due to lack of this synergistic effect. In order to maintain the nanoparticles' stability and chemical activity, the core material is also safeguarded against migration and aggregation. CSNs have been studied extensively for a variety of biological applications, including drug administration, cancer treatment, bioimaging, cell labelling, genetic engineering, methanol electrooxidation and so on [16,17]. Due to their higher surface area, superior catalytic activities and biocompatibility, CSNs have been exploited as signal amplifiers and considered promising electron modifiers to create novel sensing platforms, including electrochemical sensors and biosensors. The excellent features of CSNs make them ideal candidates for developing sensitive and novel electrochemical sensors [18–26].

Accurate, sensitive and reliable detection of H_2O_2 has received substantial attention in analytical applications due to the importance of H_2O_2 in various areas. Hydrogen peroxide is a common peroxide that is used in biological systems, medical diagnosis, environmental analysis, food and many other applications [27–29]. Furthermore, H_2O_2 as a member of reactive oxygen species (ROS), is considered one of the crucial oxidative stress biomarkers. The excessive level of H_2O_2 can cause a series of diseases such as Alzheimer's, Parkinson's, myocardial infarction, inflammatory lung diseases, cancer, etc. [30,31]. Therefore, it is essential to develop an effective method for rapid and reliable monitoring of H_2O_2 [32,33].

Several analytical methods have been developed for H_2O_2 determination, including spectrophotometry [34,35], chemiluminescence [36–38], fluorescence [39–41], chromatography [42,43] and electrochemical sensors [44–65]. However, due to the technical drawbacks of the traditional methods (low sensitivity and selectivity, laborious, time-consuming and complicated instrumentation), electrochemical sensors have received more attention due to their associated practical advantages, including high sensitivity, portability, simplicity, cost-effectiveness, rapid response time and ease of fabrication and operation. Electrochemical sensors for H_2O_2 determination are mainly based on enzymatic and non-enzymatic approaches, but due to drawbacks of enzymatic sensors such as instability (temperature, pH-related challenges), shelf-life and immobilization procedures, non-enzymatic sensors have received greater attention [44–61].

In this paper, we describe the fabrication of a hydrogen peroxide sensor based on modifying the surface of a glassy carbon electrode (GCE) with a gold@titanium dioxide ($Au@TiO_2$) core-shell nanoparticle and multi-walled carbon nanotubes. The characterization of the core-shell material and fabricated electrode was investigated thoroughly, and the electroanalytical performance of the sensor was studied and discussed in detail. The proposed sensor exhibited excellent electroanalytical performance and electrocatalytic activity toward H_2O_2 reduction. The practicality of the proposed sensor was tested by measuring H_2O_2 in human serum and saliva samples which demonstrates its potential for H_2O_2 monitoring in real-world samples. Additionally, the proposed sensor and detection strategy may offer potential prospects in electrocatalysts and electrochemical sensors development, as well as in other applications, including indicative oxidative stress monitoring, clinical diagnostics, general cancer biomarker measurements, food processing, paper bleaching and environmental analysis.

2. Materials and Methods

2.1. Materials

Gold(III) chloride hydrate ($\text{HAuCl}_4 \cdot \text{H}_2\text{O}$), trisodium citrate and multi-walled carbon nanotubes (MWCNTs) were purchased from Sigma-Aldrich. Titanium(IV) tetraisopropoxide (TTIP, 98%) and sodium dodecyl sulphate (SDS, 85%) were purchased from ACROS ORGANICS. H_2O_2 (30%) was purchased from Advent Chembio Pvt. Ltd. Potassium ferricyanide was purchased from VEB Laborchemie Apolda, while potassium ferrocyanide was purchased from BDH.

2.2. Apparatus and Measurements

The cyclic voltammetry (CV), electrochemical impedance spectroscopy (EIS) and differential pulse voltammetry (DPV) measurements were performed using CH Instruments Inc. (CHI 660D). A glassy carbon electrode (GCE, 3 mm diameter) was used as a working electrode, while a platinum wire and an Ag/AgCl reference electrode (3 M KCl) were used as counter and reference electrodes, respectively. The experiments of electrochemical characterization were carried out in 5 mM $[\text{Fe}(\text{CN})_6]^{3-/4-}$ solution as a redox probe from +0.7 V to −0.4 V, while the different concentrations of H_2O_2 (5 to 6000 μM) were prepared in 0.1 M PBS saturated with N_2 .

Raman spectroscopy was carried out using WITec alpha300 R at 532 nm. Zeta potential was measured using Malvern Zetasizer zs. Transmission electron microscopy (TEM) images were recorded using a JEOL JEM-1230. Surface morphology characterization and identification were performed using scanning electron microscopy (SEM, TESCAN VEGA3) coupled with energy dispersive X-ray analysis (EDX, BRUKER) and an atomic force microscope (5600LS, Agilent, Santa Clara, CA, USA). X-ray diffraction (XRD) was performed using an X-ray diffractometer (BRUKER, D8 DISCOVER).

2.3. Synthesis of Gold Nanoparticles (AuNPs)

Gold(III) chloride solution (147 mM, 100 μL) was added to distilled water (50 mL) to prepare 0.01% (*w/v*) solution and heated until boiling. In total, 1% (*w/v*, 2 mL) trisodium citrate was added under vigorous stirring, and the color of the solution changed from pale yellow to blue and finally red. The solution was cooled to room temperature and stored at 4 °C. The final concentration of the as-prepared gold nanoparticles was 58 ppm.

2.4. Synthesis of Core–Shell AuNPs@TiO₂ and AuNPs@TiO₂/MWCNTs

Au@TiO₂ was prepared by modifying the preparation methods mentioned in previous reports [66–68]. Au@TiO₂ with different wt% of core Au (1.09, 2.17, 4.24, 8.14 and 11.74%) was prepared. For Au@TiO₂ (8.14% Au), 20 mL of the prepared AuNPs stock solution was added dropwise to 20 mL of 0.1 mol/L SDS solution under vigorous stirring for 15 min. The mixture was centrifuged at 12,000 rpm for 10 min. The SDS-capped AuNPs were settled at the bottom of the centrifuge tube while the supernatant was removed. The SDS-capped AuNPs were washed three times with distilled water to remove the excess free SDS. In total, 50 μL of TTIP were mixed with 500 μL of isopropanol, and the mixture was added dropwise to the washed SDS-capped AuNPs under vigorous stirring. The formed precipitate was washed with ethanol and allowed to dry. The dried product was calcinated at 500 °C for 4 hrs. Then, 1 mg of AuNPs@TiO₂ was suspended in 980 μL distilled water, and 20 μL of 1 mg/mL MWCNTs were added. Finally, the mixture was sonicated for 30 min.

2.5. Fabrication of H₂O₂ Electrode (Au@TiO₂/MWCNTs/GCE)

Before making the electrochemical measurements, glassy carbon working electrodes were polished using alumina powders (1.0, 0.3 and 0.05 μm size), followed by washing with acetone and finally with deionized water and dried at room temperature. The glassy carbon electrode was firstly activated by recording CV in 0.5 M H_2SO_4 from 1.4 to −0.2 V for 20 cycles at a scan rate of 0.1 V/s. The electrode was then washed with distilled water and allowed to

dry. Then, 5 μL of the $\text{Au@TiO}_2/\text{MWCNTs}$ were drop-casted onto the electrode surface and allowed to dry at room temperature.

2.6. Real Sample Analysis

The proposed H_2O_2 sensor ($\text{Au@TiO}_2/\text{MWCNTs}/\text{GCE}$) was tested for the determination of H_2O_2 in human serum and saliva samples. Three volunteers participated in this study, two males and one female, with different ages varying from 24 to 40 years. Saliva samples were collected in the morning, volunteers were asked to rinse their mouths with water for 1 min, and then samples were collected after 3 min. Collected saliva samples were centrifuged for three minutes at 4000 rpm in order to settle down any food residues, and clear saliva was diluted 10 times with 0.1 M PBS (pH 7.4) for analysis. For the serum analysis, a 10 mL sample was collected, and the blood was allowed to coagulate for 1 h, then centrifuged at 5000 rpm for 5 min, and finally, the upper serum layer was collected and diluted 20 times with PBS for analysis.

3. Results and Discussion

3.1. UV-Visible Spectroscopy

In order to ensure the success of Au@TiO_2 preparation, UV-Visible absorption spectra were recorded for AuNPs, TiO_2 and Au@TiO_2 . As shown in Figure 1, in the case of AuNPs, the spectrum showed the characteristic absorption peak at 524 nm. TiO_2 nanoparticles are commonly used as an additive in most sunscreen formulations due to their broad absorption within the UVB and UVA region, with a maximum of 327.5 nm. The successful preparation of Au@TiO_2 was accompanied and confirmed by the disappearance of the AuNPs peak, which is attributed to the complete coverage of the core (Au) by the TiO_2 shell. Moreover, a slight blue shift was observed from 327.5 nm to 323.5 nm.

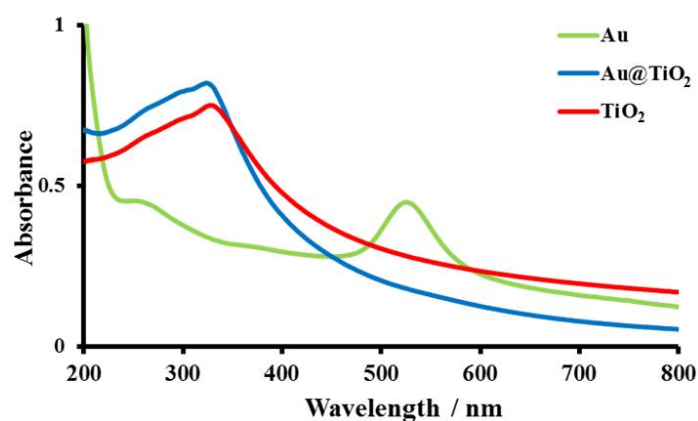


Figure 1. UV-Visible absorption spectra of AuNPs, TiO_2 and Au@TiO_2 materials.

3.2. Raman Spectroscopy

The TiO_2 and Au@TiO_2 materials were characterized by Raman spectroscopy, and the associated spectra are shown in Figure 2. The existence of bands at 144 (E_g), 198 (E_g), 396 (B_{1g}), 515 (A_{1g}) and 638 (E_g) cm^{-1} are unquestionably linked to the TiO_2 anatase phase [69–71]. In the case of Au@TiO_2 , the typical E_g peak of TiO_2 at 144 cm^{-1} shifted to a higher wavenumber (146 cm^{-1}), indicating more crystalline disorders in the anatase TiO_2 . These crystalline disorders, which developed at the point where Au and TiO_2 came into contact, impact the vibrational frequency of anatase TiO_2 and serve as traps for the produced photoelectrons.

3.3. X-ray Diffraction (XRD)

The crystalline nature of the core-shell Au@TiO_2 material was characterized by X-ray diffraction (XRD), as shown in Figure 3. The samples show two series of peaks, which can be attributed to the anatase- TiO_2 and the face-centered-cubic Au. Planes (101), (200), (105)

and (211) of anatase-TiO₂ are responsible for the peaks at 2θ of 25.7°, 44.4°, 54.0° and 54.3°, while planes (111), (200), (220) and (311) of face-centered-cubic Au are associated with the remaining peaks at 2θ of 38.2°, 44.4°, 64.7° and 77.7°, in agreement with the literature [72].

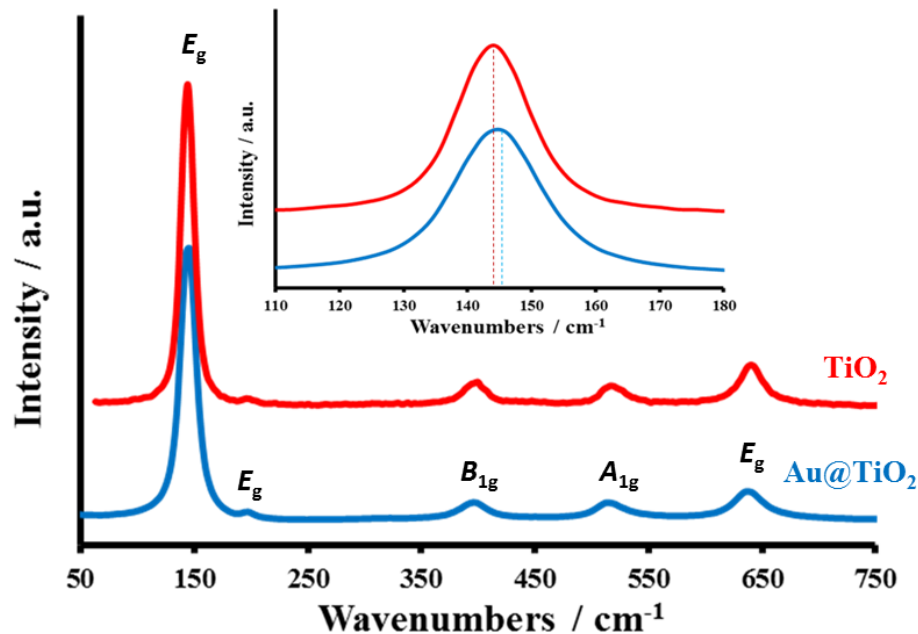


Figure 2. Raman spectra of the prepared TiO₂ and Au@TiO₂ (Au is 8.14%) materials.

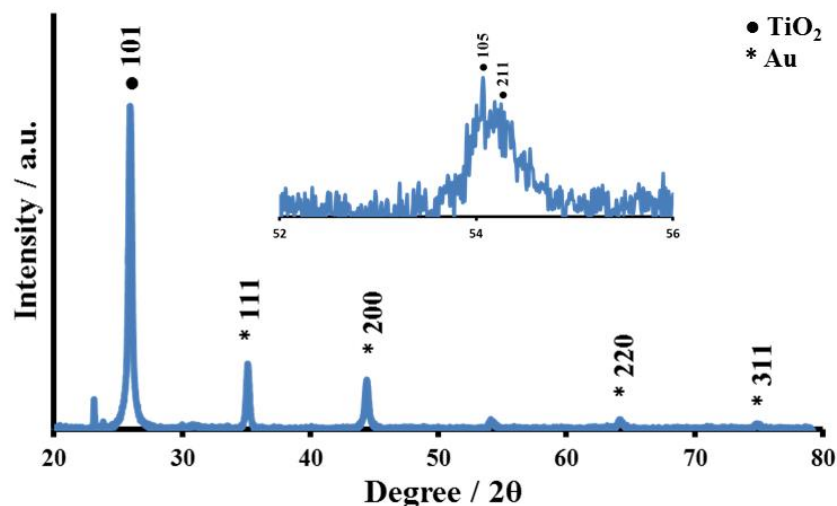


Figure 3. X-ray diffraction pattern for the prepared core-shell Au@TiO₂ material (Au = 8.14%).

3.4. Zeta-Potential Analyzer and Size Distribution

Higher zeta potential values indicate that the periphery surface charge of the nanoparticles is higher, which encourages repulsion and prevents the formation of aggregates, a sign of the stability of the core-shell nanoparticles. Au@TiO₂ core-shell with different wt% of Au (1.09, 2.17, 4.24, 8.14 and 11.74%) were prepared, and their Zeta potentials were measured to evaluate the effect of the weight percent of the core gold on the surface charge and stability of the whole core-shell material. As seen in Figure 4, the increase in the weight percent of core gold is accompanied by a positive increase in the value of Zeta potential until it reaches nearly stable values between 4.24% and 8.14%. Therefore, we decided to use 8.14% of Au content in further studies.

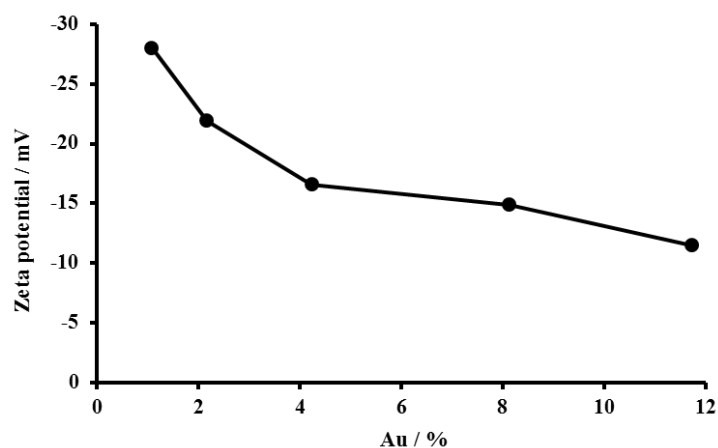


Figure 4. Zeta potential of the prepared core–shell Au@TiO₂ material with varying Au content (1.09, 2.17, 4.24, 8.14 and 11.74%).

3.5. Transmission Electron Microscopy (TEM)

TEM analysis was performed to directly measure the size, size distribution and morphology of Au@TiO₂ and Au@TiO₂/MWCNTs, which are shown in Figure 5a–d. The spherical gold nanoparticles were observed as a dark core, with about 13–15 nm diameter, in the center and totally encapsulated by a brighter shell of TiO₂. It can be observed that gold nanoparticles are well-dispersed and uniformly incorporated in the TiO₂ matrix without any significant agglomeration. Figure 5c shows the selected area electron diffraction pattern, which agrees with the XRD data and reveals that the compositions of core–shell (Au and TiO₂) reflect their signatures of crystal planes in the hybrid or composite form. The combination of MWCNTs with core–shell Au@TiO₂ is confirmed and presented in Figure 5d.

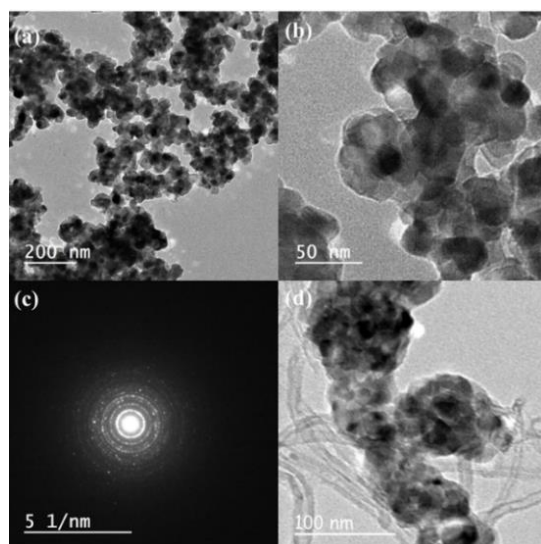


Figure 5. TEM images of (a,b) Au@TiO₂ with 8.14% Au; (c) selected area electron diffraction pattern; (d) TEM image of Au@TiO₂/MWCNTs composite material.

3.6. Scanning Electron Microscopy and Energy Dispersive X-ray Analysis (SEM and EDX)

SEM images were recorded in order to describe the surface morphology and distribution of the Au@TiO₂ material. As shown in Figure 6a,b, the presence of spherical and uniformly distributed particles was observed with a size of approximately 30.29 nm (diameter). The modification of the electrode surface with such core–shell material promises a high surface area and better electrocatalytic activity. The elemental analysis for Au@TiO₂ and

Au@TiO₂/MWCNT materials was performed, and EDX profiles are shown in Figure 6c,d. The EDX profile for Au@TiO₂/MWCNT (Figure 6d) confirms the presence of Ti, O and Au and C with a weight percent of 39.88%, 46.92%, 7.76% and 5.45%, respectively. The Au amount observed from the EDX measurements is in approximate agreement with the theoretical value of 8.14%.

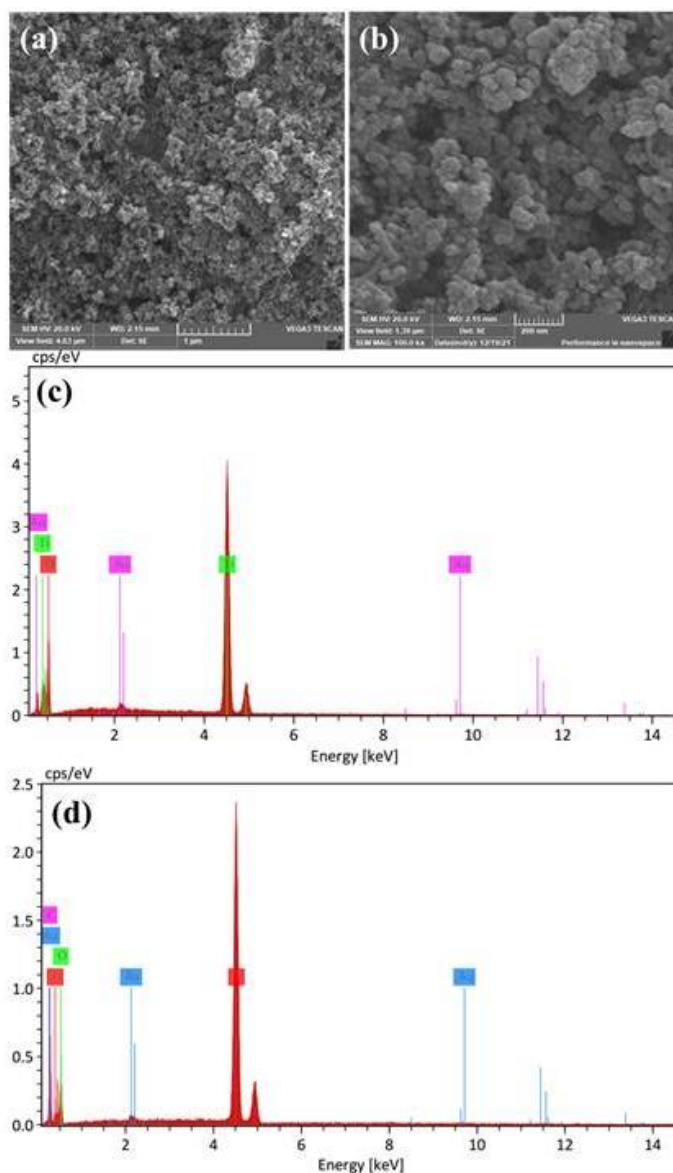


Figure 6. SEM images of Au@TiO₂ material (Au = 8.14%) at different magnifications; (a) 30 kx and (b) 100 kx. (c,d) EDX profiles for Au@TiO₂ and Au@TiO₂/MWCNT materials confirming the presence of elements as expected.

3.7. Atomic Force Microscopy (AFM)

AFM analysis was performed to characterize the surface morphology of the Au@TiO₂-modified surface, and the images are shown in Figure 7. It is obvious that the topography of the core-shell-modified surface has a high surface roughness with a root mean square height (Sq) of 35.4 nm. As shown in Figure 7a,c, the 3D images confirm the success of the core-shell preparation process. Protrusions were observed in the TiO₂ shell as the embedded gold nanoparticles in the core push the TiO₂ shell out.

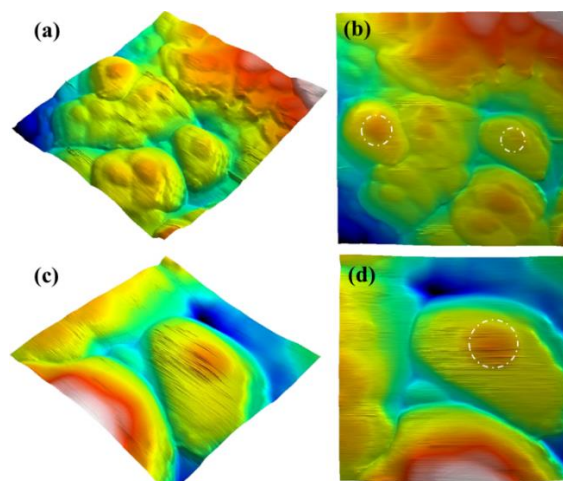


Figure 7. AFM images of the core-shell Au@TiO₂ material; (a,c) 3D images and (b,d) plane images.

3.8. Cyclic Voltammetry

Cyclic voltammetry characterization (Figure 8 and Table 1) was performed by recording the voltammograms for various stages of electrode modification in 5 mM [Fe(CN)₆]^{3−/4−} (1:1) in 0.1 M KCl at a scan rate of 100 mV/s (potential window 0.7 to −0.4 V). The current response for the MWCNTs modified electrode ($I_{\text{Oxi}} = 60.71 \mu\text{A}$ and $I_{\text{Red}} = -61.61 \mu\text{A}$, $\Delta E = 129 \text{ mV}$) was improved very significantly compared to the bare GCE ($I_{\text{Oxi}} = 45.83 \mu\text{A}$, $I_{\text{Red}} = -44.61 \mu\text{A}$, $\Delta E = 220 \text{ mV}$). This is attributed to the high conductivity of MWCNTs, which improve the electron transfer kinetics between the electrode surface and redox couple.

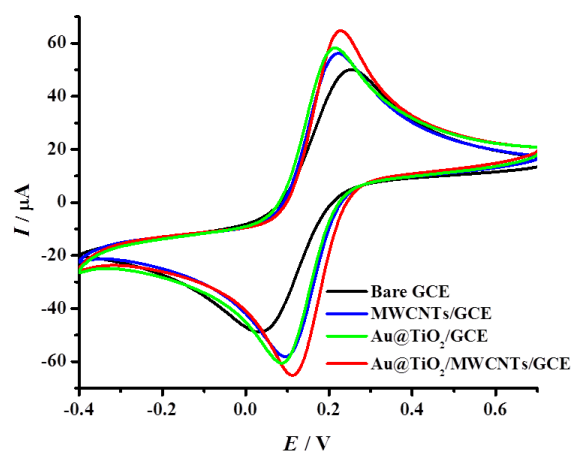


Figure 8. Cyclic voltammetric responses for bare GCE, MWCNTs/GCE, Au@TiO₂/GCE and Au@TiO₂/MWCNTs/GCE in 5 mM [Fe(CN)₆]^{3−/4−}/0.1 M KCl at a scan rate of 100 mV/s.

Table 1. CV and EIS performance data for modified and bare electrodes in [Fe(CN)₆]^{3−/4−}.

Electrode	$I_{\text{Oxi}} (\mu\text{A})$	$E (\text{mV})$	$I_{\text{Red}} (\mu\text{A})$	$E (\text{mV})$	$\Delta E (\text{mV})$	$R_s (\Omega)$	$R_{\text{ct}} (\Omega)$	$C (\mu\text{F})$	$W (\text{m}\Omega)$
Bare GCE	45.83	252	−44.61	32	220	128.4	2610	0.49	0.143
MWCNTs/GCE	60.71	223	−61.61	94	129	113.9	634	0.91	0.167
Au@TiO ₂ /GCE	61.81	213	−63.04	87	126	118.4	529	1.13	0.149
Au@TiO ₂ /MWCNTs/GCE	69.77	228	−69.56	113	115	124.8	281	1.00	0.266

The drop-casting of the as-prepared core-shell Au@TiO₂ material onto GCE also showed an increase in the current response ($I_{\text{Oxi}} = 61.81 \mu\text{A}$, $I_{\text{Red}} = -63.04 \mu\text{A}$) with a decrease in ΔE value (126 mV) and this is attributed to the combined catalytic activity of TiO₂ and Au.

Au@TiO₂/MWCNTs/GCE showed a much better current response compared to bare GCE, MWCNTs/GCE and Au@TiO₂/GCE with $I_{\text{Oxi}} = 69.77 \mu\text{A}$, $I_{\text{Red}} = -69.56 \mu\text{A}$ and the lowest ΔE (115 mV) was observed. This improvement is attributed to the synergistic effect of the core-shell Au@TiO₂ structure and the high electrical conductivity of MWCNTs.

3.9. Electrochemical Impedance Spectroscopy

EIS analysis was performed and recorded in 5 mM [Fe(CN)₆]^{3−/4−} solution at 0.22 V with a frequency range from 0.1 Hz to 10⁵ Hz (Figure 9 and Table 1) to support the cyclic voltammetry results and to confirm the R_{ct} values which agree well with the voltammetry findings. The bare GCE showed an R_{ct} of 2610 Ω, which was decreased very significantly (634 Ω) after modifying the GCE surface with MWCNTs. This is due to the reason that the electron process kinetics is faster due to the high electrical conductivity of MWCNTs, which ultimately facilitates the electron transfer and decreases the resistance. Au@TiO₂-modified GCE also showed a decrease in the R_{ct} value (529 Ω), but the proposed electrode material Au@TiO₂/MWCNTs/GCE exhibited the best and lowest charge transfer resistance (281 Ω) among all the tested materials and is attributed to the synergistic effect of the core-shell Au@TiO₂ nanostructure and high conductivity of MWCNTs.

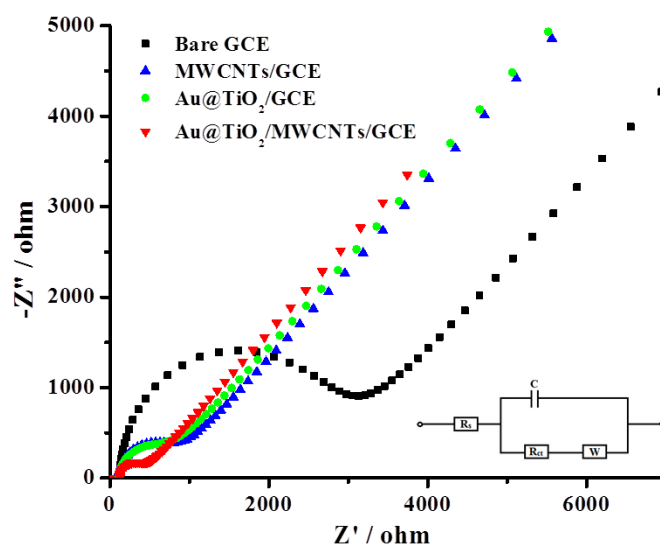


Figure 9. Nyquist plot for modified (labeled) and bare glassy carbon electrodes in 5 mM [Fe(CN)₆]^{3−/4−}/0.1 M KCl. Insert shows the Randles circuit used for data fitting.

3.10. Analytical Performance (H₂O₂ Sensing)

In order to confirm the synergistic effect on H₂O₂ sensing, DPVs were recorded in N₂-saturated PBS for the different stages of electrode modification. As shown in Figure 10, the increase in the current response was 1.5 and 1.9 times in the case of MWCNTs/GCE and Au@TiO₂/GCE, respectively, while an increase of 4.6 times was observed in the case of Au@TiO₂/MWCNTs/GCE compared to the bare glassy carbon electrode.

The DPV response of the proposed electrode (Au@TiO₂/MWCNTs/GCE) towards different H₂O₂ concentrations (PBS, pH 7.4) was recorded and shown in Figure 11. The reduction current of the hydrogen peroxide (at −0.62 V) increased with H₂O₂ concentration and showed a linear response from 5 to 200 μM ($y = -0.0046x - 0.015$) and from 200 to 6000 μM ($y = -0.0074x + 0.7217$) with coefficient of determination (R^2) of 0.9973 and 0.9994, respectively. The calculated limit of detection (LOD) was 1.4 μM based on 3σ calculations. The analytical performance of the proposed sensor was compared to other relevant and reported results and is summarized in Table 2. It is clearly evident that the proposed sensor exhibited an excellent response in terms of linear range and detection limit.

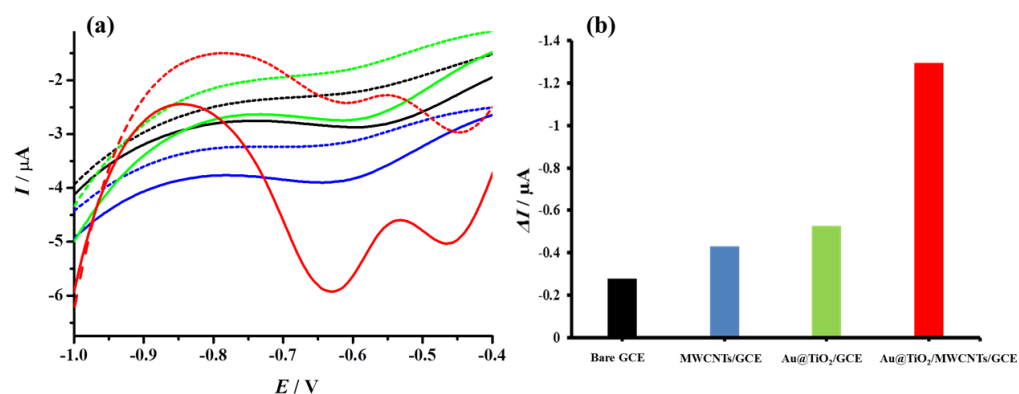


Figure 10. (a) Differential pulse voltammograms recorded in PBS (dashed lines) and 300 μM H_2O_2 (solid lines) for various stages of electrode modification, Bare GCE (black); MWCNTs/GCE (blue); Au@TiO₂/GCE (green); Au@TiO₂/MWCNTs/GCE (red). (b) Histogram represents the corresponding change in current values (ΔI).

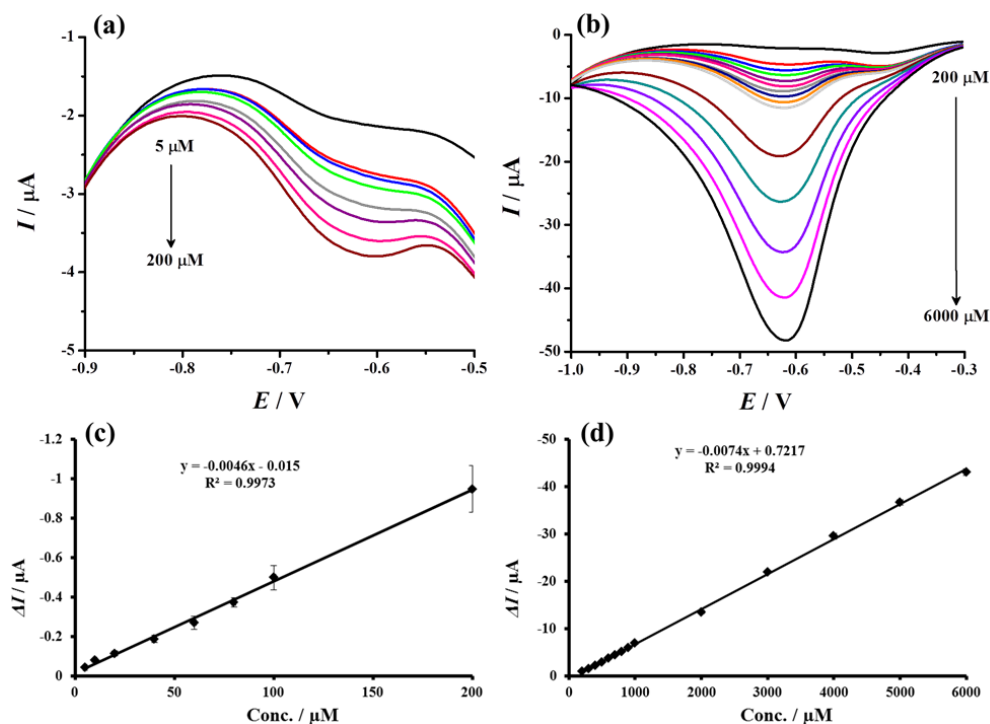


Figure 11. Differential pulse voltammograms recorded using proposed sensor (Au@TiO₂/MWCNTs/GCE towards different concentrations of H_2O_2 (a) 5 to 200 μM and (b) 200 to 6000 μM) in N_2 -saturated PBS (pH 7.4). (c,d) Corresponding calibration curves from the current responses vs. H_2O_2 concentrations plot.

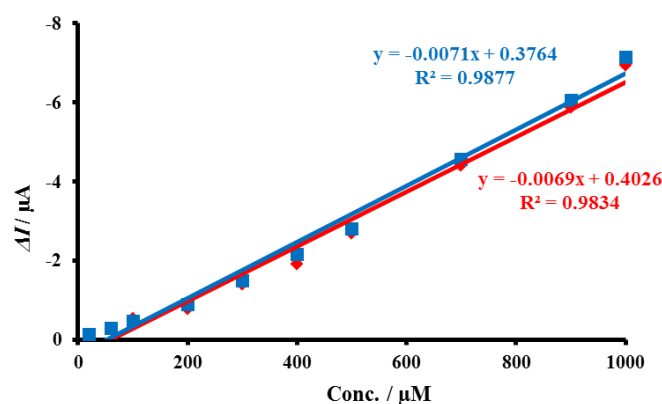
3.10.1. Stability and Reproducibility of H_2O_2 Sensor

Stability is an important parameter to describe the performance of an electrochemical sensor. The stability of the Au@TiO₂/MWCNTs/GCE sensor was investigated by measuring the current responses for different concentrations of H_2O_2 (20–1000 μM , Figure 12) after 50 days and compared with the initial response recorded. The current response for H_2O_2 after 50 days was found to be 97.1% of its initial response, and this reveals the acceptable stability and sufficient lifetime of the proposed sensor. The reproducibility of three freshly prepared Au@TiO₂/MWCNTs/GCEs was tested by measuring the current responses of 200 μM H_2O_2 , and the calculated %RSD was 4.63%.

Table 2. Comparison of the proposed sensor with the recently reported H₂O₂ sensors.

Electrode Material	Linear Range	LOD (μM)	Ref.
GO-Fe ₃ O ₄ -PAMAM-Pd/GCE	0.05–160 μM	0.01	[48]
Pd/TNM@rGO	up to 12 mM	0.0025	[49]
GQDs-CS/MB/GCE	1.0 μM –2.9 mM	0.7	[50]
Paper/CNTs/AgNPs	1 μM –700 μM	-	[51]
CuNPs-rGO	up to 18 mM	601	[52]
LSG-Ag	0.1–10 mM	7.9	[53]
α -MoO ₃ /GO/GCE	0.92 μM –2.46 mM	0.31	[54]
PtNPs@SPCEs	0–215 μM	1.9	[55]
MPS electrode	10 and 5000 μM	4.35	[56]
Pt-Pd/CFME	5–3920 μM	0.42	[57]
NiCoSe ₂ /GCE	0.05 to 402 μM	0.03	[58]
Cu@Pt/C	0.50 μM –32.56 mM	0.15	[59]
Fe ₃ O ₄ @PEI@AuNPs-GRE	0.2–500.0 μM	0.07	[60]
Cu/Cu ₂ O/FTO	0.2–2000 μM	0.04	[61]
AuNPs/n-GaN	40 μM –1 mM	10	[62]
Pd/AuNPs	0.5–6 mM	-	[63]
Ni–Bi/CC	0.1 μM –0.5 mM	0.00085	[64]
PtNP/rGO–CNT/PtNP/SPCE	25–1000 μM	4.3	[65]
Au@TiO ₂ /MWCNTs/GCE	5–200 μM and 200 μM –6 mM	1.4	This work

PAMAM: Poly(amidoamine) dendrimer; TNM: *tert*-Nonyl mercaptan; GQDs: Graphene quantum dots; CS: Chitosan; MB: Methylene blue; LSG; Laser scribed graphene; SPCEs: Screen-printed carbon electrodes; MPS: Macroporous Silicon; CFME: Carbon fiber microelectrode; PEI: Polyethyleneimine; GRE: Graphite rod electrode; FTO: Fluorine doped tin oxide; CC: Carbon cloth.

**Figure 12.** Stability study for the determination of H₂O₂ (20–1000 μM) after 50 days (red line) using the proposed sensor (Au@TiO₂/MWCNTs/GCE) compared to the response observed initially (blue line).

3.10.2. Selectivity of H₂O₂ Sensor

Possible interferences which may occur during the determination of H₂O₂ in the biological samples were examined using the proposed sensor (Au@TiO₂/MWCNTs/GCE). The interference study was performed by measuring the current response of 200 μM H₂O₂, and then the change in the current response was recorded in the presence of the common interferents (ascorbic acid, glucose, methionine, cysteine and uric acid) with 10-fold concentration (2 mM) compared to H₂O₂. As shown in Table 3, the effect of these interferents on H₂O₂ determination is expressed as a percentage recovery from the initial H₂O₂ current response (before the interferents were added). Even with such high concentrations of interferents (10-fold), the results reveal that the proposed sensor is quite selective towards H₂O₂.

Table 3. The H₂O₂ (200 µM) recovery data for the proposed electrode in the presence of common interferents (10-fold concentration, 2 mM).

Interferent (10-Folds)	Recovery (%) (n = 3)
Ascorbic acid	89.11 ± 0.50
Glucose	102.45 ± 0.87
Methionine	96.21 ± 1.23
Cysteine	105.65 ± 0.68
Uric acid	97.31 ± 0.73

3.11. Real Sample Analysis

The diluted real samples (human saliva and serum samples) were considered, and analysis was performed in triplicate for different concentrations of H₂O₂ by the standard addition method. The recovery values of the proposed sensor are shown in Table 4, which vary from 85.3 to 117.9%. The obtained results reveal that the proposed sensor exhibits a reliable response and excellent practicality for the electroanalytical determination of H₂O₂ in real biological samples.

Table 4. Application of the proposed sensor Au@TiO₂/MWCNTs/GCE for real sample analysis (human serum and saliva samples).

Sample	Added (µM)	Found in Serum (µM) (n = 3)	Recovery (%)	Found in Saliva (µM) (n = 3)	Recovery (%)
1	20	18.02 ± 0.94	90.09	18.33 ± 0.71	91.63
	40	38.10 ± 0.89	95.24	38.28 ± 0.60	95.71
	60	51.17 ± 0.70	85.29	70.74 ± 1.43	117.90
2	20	20.70 ± 1.20	103.48	21.30 ± 0.87	106.52
	40	37.41 ± 0.64	93.53	43.98 ± 0.69	109.95
	60	57.39 ± 0.56	95.65	63.85 ± 0.45	106.41
3	20	22.11 ± 0.88	110.54	22.76 ± 1.02	113.80
	40	38.10 ± 1.09	95.24	39.63 ± 0.70	99.08
	60	51.17 ± 0.79	85.29	68.30 ± 0.83	113.84

4. Conclusions

An electrochemical non-enzymatic biosensor based on Au@TiO₂ core-shell nanoparticles and multi-walled carbon nanotubes was developed and investigated for H₂O₂ determination. The success of the Au@TiO₂ preparation process was confirmed and characterized by various techniques. The different electrode modification stages were electrochemically characterized using cyclic voltammetry and electrochemical impedance spectroscopy in 5 mM [Fe(CN)₆]^{3−/4−} in order to confirm the synergistic effect of Au@TiO₂ and MWCNTs. The synergistic effect was further confirmed during differential pulse voltammetry analysis of H₂O₂ (300 µM) in 0.1 M N₂-saturated PBS (pH 7.4). The analytical performance of the modified electrode (Au@TiO₂/MWCNTs/GCE) was investigated by plotting the calibration curves of different concentrations of H₂O₂ varying from 5 to 6000 µM. The results showed that by increasing the H₂O₂ concentration, the reduction current of the hydrogen peroxide at −0.62 V increases, and the current values showed a linear response from 5 to 200 µM ($R^2 = 0.9973$) and 200 to 6000 µM ($R^2 = 0.9994$). The calculated limit of detection was 1.4 µM and attributed to the synergistic effect of Au@TiO₂ and MWCNTs.

The proposed sensor exhibited good selectivity over the possible interferents (ascorbic acid, glucose, methionine, cysteine and uric acid at a 10-fold concentration level compared to H₂O₂). The lifetime of the sensor/electrode reached 50 days with a decrease of only 2.9% of the original response (current). The developed sensor was further tested for the determination of H₂O₂ in real biological samples (human serum and saliva) using

the standard addition method. The observed response and recovery results support the potential of the proposed sensor for H₂O₂ monitoring in future real-world sample analysis.

Author Contributions: Conceptualization, M.N.A. and B.S.; methodology, A.A.S., M.N.A. and B.S.; software, A.A.S. and B.S.; validation, A.A.S., M.N.A. and B.S.; formal analysis, A.A.S.; investigation, A.A.S., M.N.A. and B.S.; resources, A.A.S., M.N.A., W.F.E.-H., Y.M.I. and B.S.; data curation, A.A.S., M.N.A. and B.S.; writing—original draft preparation, A.A.S., M.N.A. and B.S.; writing—review and editing, A.A.S., M.N.A., B.S., W.F.E.-H. and Y.M.I.; visualization, A.A.S. and B.S.; supervision, M.N.A., B.S., W.F.E.-H. and Y.M.I.; project administration, M.N.A.; funding acquisition, M.N.A. and A.A.S. All authors have read and agreed to the published version of the manuscript.

Funding: This research was partially funded by the National Research Centre (NRC, Egypt) as a PhD research support.

Informed Consent Statement: Informed consent was obtained from all subjects involved in the study.

Data Availability Statement: The data presented in this study are available on request from the corresponding author.

Acknowledgments: This paper is dedicated to the memory of Mohammed Nooredeen Abbas. We (authors) dedicate this paper to the memory of our friend ‘Mohammed Nooredeen Abbas’ (who passed away recently) and are grateful to him for his collaborative activities and contributions to the scientific community.

Conflicts of Interest: The authors declare no conflict of interest.

References

1. Lan, L.; Yao, Y.; Ping, J.; Ying, Y. Recent advances in nanomaterial-based biosensors for antibiotics detection. *Biosens. Bioelectron.* **2017**, *91*, 504–514. [[CrossRef](#)]
2. Teradal, N.L.; Jelinek, R. Carbon nanomaterials in biological studies and biomedicine. *Adv. Healthc. Mater.* **2017**, *6*, 1700574. [[CrossRef](#)]
3. Porto, L.S.; Silva, D.N.; de Oliveira, A.E.F.; Pereira, A.C.; Borges, K.B. Carbon nanomaterials: Synthesis and applications to development of electrochemical sensors in determination of drugs and compounds of clinical interest. *Rev. Anal. Chem.* **2019**, *38*, 20190017. [[CrossRef](#)]
4. Bobrinetskiy, I.I.; Knezevic, N.Z. Graphene-based biosensors for on-site detection of contaminants in food. *Anal. Methods* **2018**, *10*, 5061–5070. [[CrossRef](#)]
5. Bounegru, A.V.; Apetrei, C. Carbonaceous nanomaterials employed in the development of electrochemical sensors based on screen-printing technique—A review. *Catalysts* **2020**, *10*, 680. [[CrossRef](#)]
6. Kirchner, E.-M.; Hirsch, T. Recent developments in carbon-based two-dimensional materials: Synthesis and modification aspects for electrochemical sensors. *Microchim. Acta* **2020**, *187*, 441. [[CrossRef](#)]
7. Kour, R.; Arya, S.; Young, S.-J.; Gupta, V.; Bandhoria, P.; Khosla, A. Recent advances in carbon nanomaterials as electrochemical biosensors. *J. Electrochem. Soc.* **2020**, *167*, 037555. [[CrossRef](#)]
8. Pandey, H.; Khare, P.; Singh, S.; Singh, S.P. Carbon nanomaterials integrated molecularly imprinted polymers for biological sample analysis: A critical review. *Mater. Chem. Phys.* **2020**, *239*, 121966. [[CrossRef](#)]
9. Wang, J. Carbon-nanotube based electrochemical biosensors: A review. *Electroanal. Int. J. Devoted Fundam. Pract. Asp. Electroanal.* **2005**, *17*, 7–14. [[CrossRef](#)]
10. Nooredeen, N.M.; El-Ghaffar, A.; Darwish, W.; Elshereafy, E.; Radwan, A.; Abbas, M. Graphene oxide with covalently attached zinc monoamino-phthalocyanine coated graphite electrode as a potentiometric platform for citrate sensing in pharmaceutical preparations. *J. Solid State Electrochem.* **2015**, *19*, 2141–2154. [[CrossRef](#)]
11. Zaporotskova, I.V.; Boroznina, N.P.; Parkhomenko, Y.N.; Kozhitov, L.V. Carbon nanotubes: Sensor properties. A review. *Mod. Electron. Mater.* **2016**, *2*, 95–105. [[CrossRef](#)]
12. Norizan, M.N.; Moklis, M.H.; Demon, S.Z.N.; Halim, N.A.; Samsuri, A.; Mohamad, I.S.; Knight, V.F.; Abdullah, N. Carbon nanotubes: Functionalisation and their application in chemical sensors. *RSC Adv.* **2020**, *10*, 43704–43732. [[CrossRef](#)] [[PubMed](#)]
13. Arlyapov, V.; Kharkova, A.; Kurbanaliyeva, S.; Kuznetsova, L.; Machulin, A.; Tarasov, S.; Melnikov, P.; Ponamoreva, O.; Alferov, V.; Reshetilov, A. Use of biocompatible redox-active polymers based on carbon nanotubes and modified organic matrices for development of a highly sensitive BOD biosensor. *Enzym. Microb. Technol.* **2021**, *143*, 109706. [[CrossRef](#)]
14. Schroeder, V.; Savagatrup, S.; He, M.; Lin, S.; Swager, T.M. Carbon nanotube chemical sensors. *Chem. Rev.* **2018**, *119*, 599–663. [[CrossRef](#)] [[PubMed](#)]
15. Wang, H.; Chen, L.; Feng, Y.; Chen, H. Exploiting core-shell synergy for nanosynthesis and mechanistic investigation. *Acc. Chem. Res.* **2013**, *46*, 1636–1646. [[CrossRef](#)]

16. Core, R.G.C. Classes, Properties, Synthesis Mechanisms, Characterization, and Applications/Rajib Ghosh Chaudhuri, Santanu Paria. *Chem. Rev.* **2012**, *112*, 2373.
17. Singh, B.; Seddon, B.; Dempsey, E.; Redington, W.; Dickinson, C. Porous Core-Shell Platinum-Silver Nanocatalyst for the Electrooxidation of Methanol. *Electroanalysis* **2015**, *27*, 135–143. [[CrossRef](#)]
18. Krishnan, S.K.; Prokhorov, E.; Bahena, D.; Esparza, R.; Meyyappan, M. Chitosan-covered Pd@Pt core-shell nanocubes for direct electron transfer in electrochemical enzymatic glucose biosensor. *ACS Omega* **2017**, *2*, 1896–1904. [[CrossRef](#)]
19. Li, M.; Wang, P.; Li, F.; Chu, Q.; Li, Y.; Dong, Y. An ultrasensitive sandwich-type electrochemical immunosensor based on the signal amplification strategy of mesoporous core-shell Pd@Pt nanoparticles/ amino group functionalized graphene nanocomposite. *Biosens. Bioelectron.* **2017**, *87*, 752–759. [[CrossRef](#)]
20. Wang, R.; Liu, W.-D.; Wang, A.-J.; Xue, Y.; Wu, L.; Feng, J.-J. A new label-free electrochemical immunosensor based on dendritic core-shell AuPd@ Au nanocrystals for highly sensitive detection of prostate specific antigen. *Biosens. Bioelectron.* **2018**, *99*, 458–463. [[CrossRef](#)]
21. Zhang, X.; Li, Y.; Lv, H.; Feng, J.; Gao, Z.; Wang, P.; Dong, Y.; Liu, Q.; Zhao, Z. Sandwich-type electrochemical immunosensor based on Au@Ag supported on functionalized phenolic resin microporous carbon spheres for ultrasensitive analysis of α -fetoprotein. *Biosens. Bioelectron.* **2018**, *106*, 142–148. [[CrossRef](#)] [[PubMed](#)]
22. Yang, F.; Yang, Z.; Zhuo, Y.; Chai, Y.; Yuan, R. Ultrasensitive electrochemical immunosensor for carbohydrate antigen 19-9 using Au/porous graphene nanocomposites as platform and Au@Pd core/shell bimetallic functionalized graphene nanocomposites as signal enhancers. *Biosens. Bioelectron.* **2015**, *66*, 356–362. [[CrossRef](#)] [[PubMed](#)]
23. Xu, W.; Yi, H.; Yuan, Y.; Jing, P.; Chai, Y.; Yuan, R.; Wilson, G.S. An electrochemical aptasensor for thrombin using synergetic catalysis of enzyme and porous Au@Pd core-shell nanostructures for signal amplification. *Biosens. Bioelectron.* **2015**, *64*, 423–428. [[CrossRef](#)] [[PubMed](#)]
24. Tabrizi, M.A.; Shamsipur, M.; Saber, R.; Sarkar, S.; Sherkatkhameneh, N. Flow injection amperometric sandwich-type electrochemical aptasensor for the determination of adenocarcinoma gastric cancer cell using aptamer-Au@Ag nanoparticles as labeled aptamer. *Electrochim. Acta* **2017**, *246*, 1147–1154. [[CrossRef](#)]
25. Mazloum-Ardakani, M.; Hosseinzadeh, L.; Taleat, Z. Synthesis and electrocatalytic effect of Ag@Pt core-shell nanoparticles supported on reduced graphene oxide for sensitive and simple label-free electrochemical aptasensor. *Biosens. Bioelectron.* **2015**, *74*, 30–36. [[CrossRef](#)] [[PubMed](#)]
26. Wang, M.; Hu, B.; Ji, H.; Song, Y.; Liu, J.; Peng, D.; He, L.; Zhang, Z. Aptasensor based on hierarchical core-shell nanocomposites of zirconium hexacyanoferrate nanoparticles and mesoporous mFe₃O₄@ mC: Electrochemical quantitation of epithelial tumor marker Mucin-1. *ACS Omega* **2017**, *2*, 6809–6818. [[CrossRef](#)]
27. Bai, J.; Jiang, X. A facile one-pot synthesis of copper sulfide-decorated reduced graphene oxide composites for enhanced detecting of H₂O₂ in biological environments. *Anal. Chem.* **2013**, *85*, 8095–8101. [[CrossRef](#)]
28. Rhee, S.G. H₂O₂, a necessary evil for cell signaling. *Science* **2006**, *312*, 1882–1883. [[CrossRef](#)]
29. Wu, W.; Li, J.; Chen, L.; Ma, Z.; Zhang, W.; Liu, Z.; Cheng, Y.; Du, L.; Li, M. Bioluminescent probe for hydrogen peroxide imaging in vitro and in vivo. *Anal. Chem.* **2014**, *86*, 9800–9806. [[CrossRef](#)]
30. Hang, T.; Xiao, S.; Yang, C.; Li, X.; Guo, C.; He, G.; Li, B.; Yang, C.; Chen, H.-j.; Liu, F.; et al. Hierarchical graphene/nanorods-based H₂O₂ electrochemical sensor with self-cleaning and anti-biofouling properties. *Sens. Actuators B Chem.* **2019**, *289*, 15–23. [[CrossRef](#)]
31. Dong, Y.; Zheng, J. Environmentally friendly synthesis of Co-based zeolitic imidazolate framework and its application as H₂O₂ sensor. *Chem. Eng. J.* **2020**, *392*, 123690. [[CrossRef](#)]
32. Shang, L.; Zeng, B.; Zhao, F. Fabrication of novel nitrogen-doped graphene-hollow AuPd nanoparticle hybrid films for the highly efficient electrocatalytic reduction of H₂O₂. *ACS Appl. Mater. Interfaces* **2015**, *7*, 122–128. [[CrossRef](#)] [[PubMed](#)]
33. Yang, K.; Zhong, H.; Cheng, Z.; Li, X.; Zhang, A.; Li, T.; Zhang, Y.; Liu, G.; Qian, H. Magnetic Fe₃O₄ stacked sphere-like nanocomposite and its application as platform for H₂O₂ sensing. *J. Electroanal. Chem.* **2018**, *814*, 1–6. [[CrossRef](#)]
34. Nagaraja, P.; Prakash, J.; Asha, S.; Bhaskara, B.; Kumar, S.A. Dibenzazepin hydrochloride as a new spectrophotometric reagent for determination of hydrogen peroxide in plant extracts. *Environ. Monit. Assess.* **2012**, *184*, 5983–5988. [[CrossRef](#)]
35. Hoshino, M.; Kamino, S.; Doi, M.; Takada, S.; Mitani, S.; Yanagihara, R.; Asano, M.; Yamaguchi, T.; Fujita, Y. Spectrophotometric determination of hydrogen peroxide with osmium(VIII) and m-carboxyphenylfluorone. *Spectrochim. Acta Part A Mol. Biomol. Spectrosc.* **2014**, *117*, 814–816. [[CrossRef](#)]
36. Jamil, L.A.; Faizullah, A.T.; Saleem, P.H. Flow Injection Analysis of Hydrogen Peroxide with Peroxyoxalate Chemiluminescence Detection. *Sci. J. Univ. Zakho* **2017**, *5*, 88–92. [[CrossRef](#)]
37. Yu, D.; Wang, P.; Zhao, Y.; Fan, A. Iodophenol blue-enhanced luminol chemiluminescence and its application to hydrogen peroxide and glucose detection. *Talanta* **2016**, *146*, 655–661. [[CrossRef](#)]
38. Wang, K.; Liu, Q.; Wu, X.-Y.; Guan, Q.-M.; Li, H.-N. Graphene enhanced electrochemiluminescence of CdS nanocrystal for H₂O₂ sensing. *Talanta* **2010**, *82*, 372–376. [[CrossRef](#)]
39. Sasakura, K.; Hanaoka, K.; Shibuya, N.; Mikami, Y.; Kimura, Y.; Komatsu, T.; Ueno, T.; Terai, T.; Kimura, H.; Nagano, T. Development of a highly selective fluorescence probe for hydrogen sulfide. *J. Am. Chem. Soc.* **2011**, *133*, 18003–18005. [[CrossRef](#)]
40. Xu, M.; Han, J.-M.; Wang, C.; Yang, X.; Pei, J.; Zang, L. Fluorescence ratiometric sensor for trace vapor detection of hydrogen peroxide. *ACS Appl. Mater. Interfaces* **2014**, *6*, 8708–8714. [[CrossRef](#)]

41. Chang, J.; Li, H.; Hou, T.; Duan, W.; Li, F. Paper-based fluorescent sensor via aggregation induced emission fluorogen for facile and sensitive visual detection of hydrogen peroxide and glucose. *Biosens. Bioelectron.* **2018**, *104*, 152–157. [[CrossRef](#)] [[PubMed](#)]
42. Tarvin, M.; McCord, B.; Mount, K.; Sherlach, K.; Miller, M.L. Optimization of two methods for the analysis of hydrogen peroxide: High performance liquid chromatography with fluorescence detection and high performance liquid chromatography with electrochemical detection in direct current mode. *J. Chromatogr. A* **2010**, *1217*, 7564–7572. [[CrossRef](#)] [[PubMed](#)]
43. Hu, H.-C.; Jin, H.-J.; Chai, X.-S. Rapid determination of hydrogen peroxide in pulp bleaching effluents by headspace gas chromatography. *J. Chromatogr. A* **2012**, *1235*, 182–184. [[CrossRef](#)] [[PubMed](#)]
44. Yu, G.; Wu, W.; Pan, X.; Zhao, Q.; Wei, X.; Lu, Q. High Sensitive and Selective Sensing of Hydrogen Peroxide Released from Pheochromocytoma Cells Based on Pt-Au Bimetallic Nanoparticles Electrodeposited on Reduced Graphene Sheets. *Sensors* **2015**, *15*, 2709–2722. [[CrossRef](#)]
45. He, G.; Gao, F.; Li, W.; Li, P.; Zhang, X.; Yin, H.; Yang, B.; Liu, Y.; Zhang, S. Electrochemical sensing of H₂O₂ released from living cells based on AuPd alloy-modified PDA nanotubes. *Anal. Methods* **2019**, *11*, 1651–1656. [[CrossRef](#)]
46. Dai, H.; Lü, W.; Zuo, X.; Zhu, Q.; Pan, C.; Niu, X.; Liu, J.; Chen, H.; Chen, X. A novel biosensor based on boronic acid functionalized metal-organic frameworks for the determination of hydrogen peroxide released from living cells. *Biosens. Bioelectron.* **2017**, *95*, 131–137. [[CrossRef](#)]
47. Xi, J.; Xie, C.; Zhang, Y.; Wang, L.; Xiao, J.; Duan, X.; Ren, J.; Xiao, F.; Wang, S. Pd nanoparticles decorated N-doped graphene quantum dots@N-doped carbon hollow nanospheres with high electrochemical sensing performance in cancer detection. *ACS Appl. Mater. Interfaces* **2016**, *8*, 22563–22573. [[CrossRef](#)]
48. Baghayeri, M.; Alinezhad, H.; Tarahomi, M.; Fayazi, M.; Ghanei-Motlagh, M.; Maleki, B. A non-enzymatic hydrogen peroxide sensor based on dendrimer functionalized magnetic graphene oxide decorated with palladium nanoparticles. *Appl. Surf. Sci.* **2019**, *478*, 87–93. [[CrossRef](#)]
49. Bozkurt, S.; Tosun, B.; Sen, B.; Akocak, S.; Savk, A.; Ebeoğlu, M.F.; Sen, F. A hydrogen peroxide sensor based on TNM functionalized reduced graphene oxide grafted with highly monodisperse Pd nanoparticles. *Anal. Chim. Acta* **2017**, *989*, 88–94. [[CrossRef](#)]
50. Mollarasouli, F.; Asadpour-Zeynali, K.; Campuzano, S.; Yáñez-Sedeño, P.; Pingarrón, J.M. Non-enzymatic hydrogen peroxide sensor based on graphene quantum dots-chitosan/methylene blue hybrid nanostructures. *Electrochim. Acta* **2017**, *246*, 303–314. [[CrossRef](#)]
51. Shamkhalichenar, H.; Choi, J.-W. An inkjet-printed non-enzymatic hydrogen peroxide sensor on paper. *J. Electrochem. Soc.* **2017**, *164*, B3101–B3106. [[CrossRef](#)]
52. Nia, P.M.; Woi, P.M.; Alias, Y. Facile one-step electrochemical deposition of copper nanoparticles and reduced graphene oxide as nonenzymatic hydrogen peroxide sensor. *Appl. Surf. Sci.* **2017**, *413*, 56–65.
53. Aparicio-Martínez, E.; Ibarra, A.; Estrada-Moreno, I.A.; Osuna, V.; Dominguez, R.B. Flexible electrochemical sensor based on laser scribed Graphene/Ag nanoparticles for non-enzymatic hydrogen peroxide detection. *Sens. Actuators B Chem.* **2019**, *301*, 127101. [[CrossRef](#)]
54. Li, B.; Song, H.-Y.; Deng, Z.-P.; Huo, L.-H.; Gao, S. Novel sensitive amperometric hydrogen peroxide sensor using layered hierarchical porous α -MoO₃ and GO modified glass carbon electrode. *Sens. Actuators B Chem.* **2019**, *288*, 641–648. [[CrossRef](#)]
55. Agrisuelas, J.; González-Sánchez, M.-I.; Valero, E. Hydrogen peroxide sensor based on in situ grown Pt nanoparticles from waste screen-printed electrodes. *Sens. Actuators B Chem.* **2017**, *249*, 499–505. [[CrossRef](#)]
56. Al-Hardan, N.H.; Abdul Hamid, M.A.; Shamsudin, R.; Al-Khalqi, E.M.; Kar Keng, L.; Ahmed, N.M. Electrochemical hydrogen peroxide sensor based on macroporous silicon. *Sensors* **2018**, *18*, 716. [[CrossRef](#)]
57. Li, H.; Zhao, H.; He, H.; Shi, L.; Cai, X.; Lan, M. Pt-Pd bimetallic nanocoral modified carbon fiber microelectrode as a sensitive hydrogen peroxide sensor for cellular detection. *Sens. Actuators B Chem.* **2018**, *260*, 174–182. [[CrossRef](#)]
58. Sakthivel, M.; Sukanya, R.; Chen, S.-M.; Pandi, K.; Ho, K.-C. Synthesis and characterization of bimetallic nickel-cobalt chalcogenides (NiCoSe₂, NiCo₂S₄, and NiCo₂O₄) for non-enzymatic hydrogen peroxide sensor and energy storage: Electrochemical properties dependence on the metal-to-chalcogen composition. *Renew. Energy* **2019**, *138*, 139–151. [[CrossRef](#)]
59. Zhao, W.; Jin, J.; Wu, H.; Wang, S.; Fneg, C.; Yang, S.; Ding, Y. Electrochemical hydrogen peroxide sensor based on carbon supported Cu@Pt core-shell nanoparticles. *Mater. Sci. Eng. C* **2017**, *78*, 185–190. [[CrossRef](#)]
60. Ghanei-Motlagh, M.; Hosseinifar, A. A novel amperometric hydrogen peroxide sensor based on gold nanoparticles supported on Fe₃O₄@polyethyleneimine. *Int. J. Environ. Anal. Chem.* **2020**, *100*, 591–601. [[CrossRef](#)]
61. Han, L.; Tang, L.; Deng, D.; He, H.; Zhou, M.; Luo, L. A novel hydrogen peroxide sensor based on electrodeposited copper/cuprous oxide nanocomposites. *Analyst* **2019**, *144*, 685–690. [[CrossRef](#)] [[PubMed](#)]
62. Ma, C.; Yang, C.; Zhang, M. A novel electrochemical hydrogen peroxide sensor based on AuNPs/n-type GaN electrode. *Chem. Lett.* **2020**, *49*, 656–658. [[CrossRef](#)]
63. Banerjee, S.; Hossain, M.F.; Slaughter, G. A Highly Sensitive Non-Enzymatic Hydrogen Peroxide Sensor based on Palladium-Gold Nanoparticles. In Proceedings of the 2020 IEEE 15th International Conference on Nano/Micro Engineered and Molecular System (NEMS), San Diego, CA, USA, 27–30 September 2020; pp. 286–289.
64. Wang, Z.; Xie, F.; Liu, Z.; Du, G.; Asiri, A.M.; Sun, X. High-performance non-enzyme hydrogen peroxide detection in neutral solution: Using a nickel borate nanoarray as a 3D electrochemical sensor. *Chem. Eur. J.* **2017**, *23*, 16179–16183. [[CrossRef](#)] [[PubMed](#)]

65. Lee, S.; Lee, Y.J.; Kim, J.H.; Lee, G.-J. Electrochemical Detection of H₂O₂ Released from Prostate Cancer Cells Using Pt Nanoparticle-Decorated rGO–CNT Nanocomposite-Modified Screen-Printed Carbon Electrodes. *Chemosensors* **2020**, *8*, 63. [[CrossRef](#)]
66. Oh, J.T.; Chowdhury, S.R.; Lee, T.L.; Misra, M. Synergetic influence of Au/Cu₂O core-shells nanoparticle on optical, photo-electrochemical, and catalytic activities of Au/Cu₂O/TiO₂ nanocomposite. *Dye. Pigment.* **2019**, *160*, 936–943. [[CrossRef](#)]
67. Chen, T.-M.; Xu, G.-Y.; Ren, H.; Zhang, H.; Tian, Z.-Q.; Li, J.-F. Synthesis of Au@TiO₂ core–shell nanoparticles with tunable structures for plasmon-enhanced photocatalysis. *Nanoscale Adv.* **2019**, *1*, 4522–4528. [[CrossRef](#)]
68. Goebel, J.; Joo, J.B.; Dahl, M.; Yin, Y. Synthesis of tailored Au@TiO₂ core–shell nanoparticles for photocatalytic reforming of ethanol. *Catal. Today* **2014**, *225*, 90–95. [[CrossRef](#)]
69. Sun, H.; He, Q.; Zeng, S.; She, P.; Zhang, X.; Li, J.; Liu, Z. Controllable growth of Au@TiO₂ yolk–shell nanoparticles and their geometry parameter effects on photocatalytic activity. *New J. Chem.* **2017**, *41*, 7244–7252. [[CrossRef](#)]
70. Wang, Y.; Yang, C.; Chen, A.; Pu, W.; Gong, J. Influence of yolk-shell Au@TiO₂ structure induced photocatalytic activity towards gaseous pollutant degradation under visible light. *Appl. Catal. B Environ.* **2019**, *251*, 57–65. [[CrossRef](#)]
71. Baba, K.; Bulou, S.; Quesada-Gonzalez, M.; Bonot, S.; Collard, D.; Boscher, N.D.; Choquet, P. Significance of a noble metal nanolayer on the UV and visible light photocatalytic activity of anatase TiO₂ thin films grown from a scalable PECVD/PVD approach. *ACS Appl. Mater. Interfaces* **2017**, *9*, 41200–41209. [[CrossRef](#)]
72. Sun, H.; He, Q.; She, P.; Zeng, S.; Xu, K.; Li, J.; Liang, S.; Liu, Z. One-pot synthesis of Au@TiO₂ yolk-shell nanoparticles with enhanced photocatalytic activity under visible light. *J. Colloid Interface Sci.* **2017**, *505*, 884–891. [[CrossRef](#)] [[PubMed](#)]